Numerical Correlation of Heat Transfer From an Array of Hot-Air Jets Impinging on 3D Concave Surface

Mathieu Fregeau*, F. Saeed†, I. Paraschivoiu‡

École Polytechnique de Montréal, Département de Génie Mécanique
CP 6079, Succ. Centre-Ville, Montréal, Québec, H3C 3A7, Canada

King Fahd University of Petroleum and Minerals
Mail Box 1637, Dhahran 31261, Saudi Arabia

ABSTRACT

The paper presents numerical heat-transfer correlations established from numerical CFD study of a 3D hot-air jet array impinging on curved (circular) surface. The results are in the form of numerical correlations for the average and maximum Nusselt number for different nozzle-to-nozzle spacing, nozzle-to-surface height and hot-air jet mach numbers typical of those in an hot-air anti-icing system employed on aircraft wings. The paper presents a validation case and show that the results obtained from the CFD study are in good agreement with experimental data found in literature. The paper presents an interpolation technique, the dual Kriging method, that make use of the numerical database for anti-icing simulation on aircraft wings. The benefit of using the dual Kriging method is that it preserves the non-linear nature of the heat-transfer distribution from a hot-air jet impinging on a curved surface.

NOMENCLATURE

a_i	= derivative function coefficient
$c_1 \ldots c_8$	= correlation coefficient
C_p	= specific heat at constant pressure
d	= piccolo hole (jet) diameter
G	= mass-flow rate of air per unit area, $\frac{\dot{m}}{S}$
H	= nozzle-to-surface distance
h_c	= heat transfer coefficient
h_{ave}	= average heat transfer coefficient
h	= eucledian's distance
I	= identity Matrix
k	= thermal conductivity
K	= generalized covariance term
Nu	= Nusselt number based on jet dia., $\frac{h_c d}{k}$
Re	= Reynolds number, $\frac{V_{jet} d}{\nu}$
$\dot{m}$	= mass-flow rate of air, $\rho_{jet} A_{noz} V_{jet}$
M	= Mach number
n	= number of samples per variable
N	= number of variables
Pr	= Prandlt number, $\frac{C_p \mu}{k}$
$\dot{q}$	= heat flux
S	= reference surface area
s	= coordinate along surface with origin at center of jet axis, $y = 0$ plane
T	= temperature, K
U	= general function
V_{jet}	= mean jet velocity at exit of piccolo tube
W	= nozzle-to-nozzle distance
X	= multi-variable sampling
x	= one variable sampling
x, y, z	= coordinate system with origin at center of jet exit
Γ	= Kriging matrix
$\hat{\Gamma}$	= weighted Kriging matrix
μ	= dynamic viscosity
ν	= kinematic viscosity, μ/ρ
ρ	= fluid density

*Graduate Research Student. AIAA Member.
†Assistant Professor. AIAA Member.
‡Bombardier Aeronautical Chair Professor. AIAA Associate Fellow.

σ = weight value
Φ = derivative function
Ψ = covariance function
Superscripts:
$(\tilde{\ })$ = interpolated function or variables from which we interpolate
Subscripts:
$(_{anti})$ = from the anti-icing system
$(_{ave})$ = averaged
$(_{jet})$ = at the exit of piccolo tube (jet condition)
$(_{max})$ = at the maximum point of the indexed variable
$(_{s})$ = at the surface

Introduction

Icing condition is a real potential hazard during climb and descent of aircraft. As the aerodynamics performance are seriously altered when ice accretes on wings; stalling or losing command of control surface can cause serious safety deficiencies. To enhance flight safety under natural icing conditions, one of the several key tasks outlined in the FAA In-Flight Aircraft Icing Plan is to ensure the validity and reliability of icing simulation and modeling methods currently being used and developed [1, 2]. In an effort to support the objectives of the FAA Icing Plan, and facilitate Bombardier Aerospace in the certification process, the main focus of research under the J.-A. Bombardier Aeronautical Chair at École Polytechnique, Montreal, has been the development of a reliable ice accretion and anti-icing simulation code CANICE [3, 4, 5, 6, 7, 8]. The development of CANICE has been geared towards the specific needs of Bombardier Aerospace. The anti-icing simulation is commonly used on the Bombardier Aerospace regional jets — hot-air anti-icing system. The anti-icing system uses hot air from the engine compressor bleed. A system of external mounted ice detectors with a sensing probe oscillating with a set frequency, that decreases as ice accumulates on the surface, act as a warning system.

The focus of the present study is on the heat transfer distribution on the leading edge internal surface when anti-icing system is used; that is, an array of round hot-air and high-speed jets. A review of literature reveals that only few experimental and theoretical/numerical studies have been carried out to study the heat-transfer and flow in the internal hot-air region [9, 10, 11, 12, 13]. These studies have focused on specific concerns that neither address the issues related to the design of a hot-air anti-icing system nor highlight variables that might play an important part in an optimum design of such a system. A numerical model using flat plate as impingement surface has previously been implemented into CANICE code and has shown lack of accuracy in heat transfer far from impingement point [14, 10]. Hence a need for an in-depth analysis of a hot-air anti-icing system becomes significant.

Numerical simulation using CFD has become a reliable tool to fill the gap left by a lack of experimental data. Therefore, this study was conducted using state-of-the-art commercial CFD software, FLUENT. The main goal was to use CFD to determine the local Nusselt number distribution on a concave surface from an array of hot-air jets. The local Nusselt number distribution $Nu(s, y)$ is determined for various values of Mach number, nozzle-to-surface height and nozzle-to-nozzle spacing, for the particular case of a singular array of round-shaped nozzle. On the basis of the numerical prediction, a correlation is established in order to interpolate the local Nusselt number, the Nu_{ave} and Nu_{max} within the range of the domain of study.

The reader is invited to review a previous study which presents all details about numerical simulation modeling and results [15]* Some brief details of the CFD modeling, results and a validation case will, however, be reviewed for comprehension.

Exponential based numerical correlation will be derived from the parametrized variables.

*Although the reference cited is a conference proceeding, the reader is invited to consult the Canadian Aeronautical and Space Journal for the complete article, to be published shortly.

Kriging interpolation technique is being used for implementation in CANICE-3D Anti-Icing module and will be described. Results of the Kriging interpolation implementation will be presented and discussed.

Numerical Study

For a generic single array of round hot-air jets impinging on a curved surface, the local Nusselt number distribution can be expressed as:

$$Nu = f(\frac{s}{d}, \frac{y}{d}, M_{jet}, \frac{H}{d}, \frac{W}{d}) \qquad (1)$$

Considering a constant temperature of 400K for the hot-air jet and a circular shaped impingement surface, the distance H is used as the nozzle-to-surface distance as well as the radius of the arc of the curved surface. Although the leading edge profile of an aircraft wing is not a perfect circular shape, the use of a circular profile is by far the best model that can be used for parametric representation and analytical model. In addition, a single array and a constant nozzle diameter of 2.5mm was selected. The temperature upon the impingement surface was kept constant at 260K. Fig. (1) shows the coordinate reference frame used and Fig. (2) sketch the geometric parameters used for the anti-icing model.

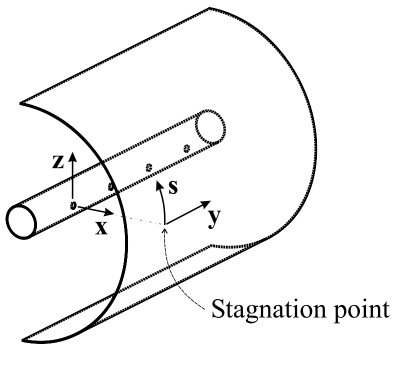

Figure 1: Coordinate system used for the anti-icing system modeling

Nine different geometric configurations have been simulated at three different jet Mach number conditions. All cases examined in the study are listed in Table (1).

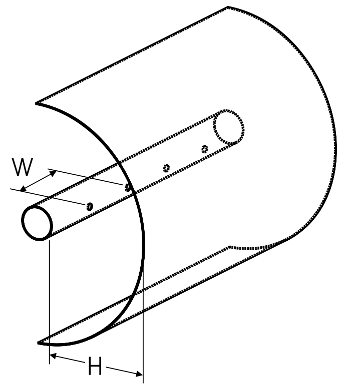

Figure 2: Geometric parameters

Table 1: Geometric characteristics and operating conditions used in this study.

Variables	Values		
Jet Mach number, M_{jet}	0.4	0.6	0.8
Height-to-dia. ratio, $\frac{H}{d}$	5	10	15
Jet spacing-to-dia. ratio, $\frac{W}{d}$	7.5	15	22.5

The numerical simulation of the 3D internal hot-air flow has been conducted using FLUENT commercial CFD package (V6.0.20). FLUENT code can simulate a large variety of flow problems from subsonic to hypersonic viscous and inviscid conditions. Many of the turbulent models are encoded with some variable coefficients and wall-laws; however, you can add your own function that rules most variables [16].

As the high compressibility of the flow and high Reynolds implies region of high velocity gradients, the Spalart-Allmaras turbulence model was used. This single, vorticity based turbulence equation model keeps the resolution at a low level of complexity. In all cases, boundary layer mesh was kept constant to ensure a y^+ below 1. Fig. (3) shows a typical mesh. There was concentration near exit of piccolo hole as well as near the impingement region. First cell height was $3e-5$ on those region, as shown on Figs. (4) and (5).

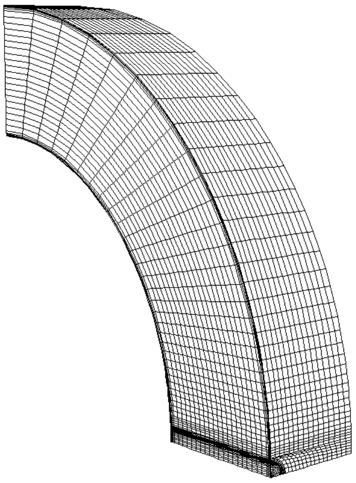

Figure 3: Structured mesh used

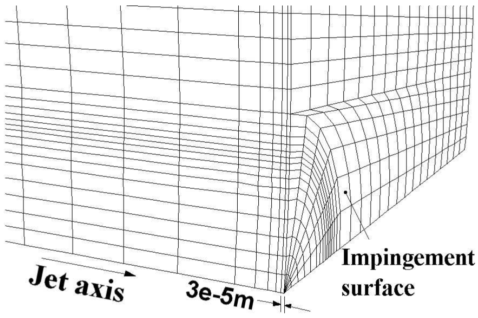

Figure 4: Mesh concentration near impact surface, exterior view

Validation Case

In order to establish the validity of our CFD model, the Gardon and Cobonpue study has been used for comparison [17]. This experimental study uses flat plate as the impingement surface. A similar numerical 3D model of linear array of jets impinging on a flat plate was examined. A summary of input conditions for the validation case is listed in Table (2). The boundary layer mesh near the exit hole has been set to ensure a ${y^+}_{max}$ below 1 on all surfaces. Fig. (6) shows the mesh used for the validation case.

The local Nusselt number distribution across the surface was determined numerically and is

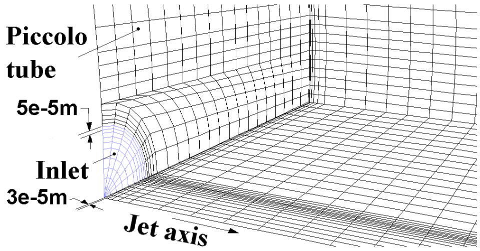

Figure 5: Mesh concentration near inlet, interior view

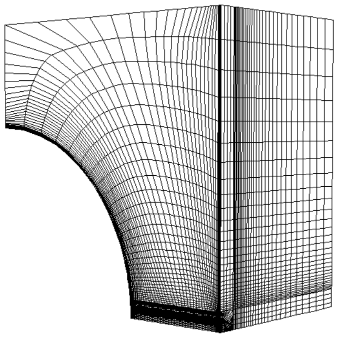

Figure 6: Mesh used for validation case

plotted in Fig. (7) along surface length axis with the empirical results of Gardon and Cobonpue [17]. As evident from Fig. (7) the predicted local Nusselt number distribution shows good agreement with empirical ones. The first 5% of s/d shows higher heat transfer from the numerical results, which can be attributed to the use of 1st order spatial discretization scheme [15]. Next $5 - 20\%$ of the s/d range shows sharp agreement while the remaining 80% shows an increase in the error, having a continuous lower local Nusselt for the numerical part. Using a rectangular shaped array for the experimental study instead of a linear array would suggest less energy dissipation far from the stagnation point for the experimental part.

Numerical Correlation

The averaged heat transfer coefficient per unit area h_{ave} is retrieved by integrating the local heat transfer coefficient over a reference surface S divided by this reference surface area,

Table 2: Operating conditions used for validation.

Variable	Value
Jet Mach number, M_{jet}	0.4
Jet height-to-diameter ratio, $\frac{H}{d}$	6
Jet spacing-to-diameter ratio, $\frac{W}{d}$	20.0
Hole Diameter, d	6.35mm
ΔT $(T_{jet} - T_s)$	20K

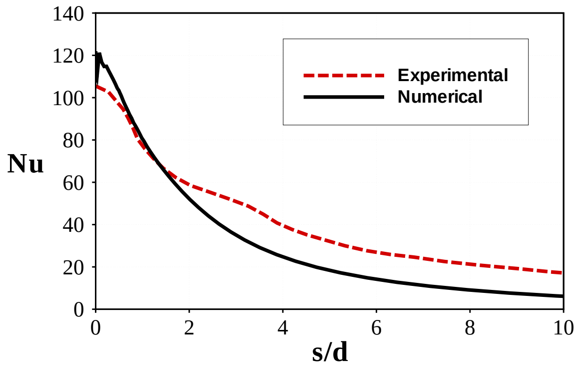

Figure 7: Heat transfer distribution from jets impinging on a flat plate

as per eq. (2).

$$\overline{h_c} = \frac{1}{S}\oint_S h_c\, ds \quad (2)$$

$$\text{Where} \quad S = \frac{\pi}{2}(HW)\frac{H}{d}\left(\frac{W}{d}\right)^{3/2} \quad (3)$$

Averaged Nusselt number, Nu_{ave}, related to the mass-flow Reynolds number Re_G presents a correlation factor, R^2, of 0.9901, using a power-law least squares technique, eq. (4). The Reynolds number, Re_G, considers the mass-flow per unit area, and the parameter H, under equation (6). Correlation is shown on Fig. (8).

$$\overline{Nu} = 10^{-10} {Re_G}^{1.1131} \quad (4)$$

$$\text{Where} \quad \overline{Nu} = \frac{\overline{h_c} H}{k} \quad (5)$$

$$Re_G = \frac{G}{d\mu HW} \quad (6)$$

$$G = \frac{\dot{m}}{S} \quad (7)$$

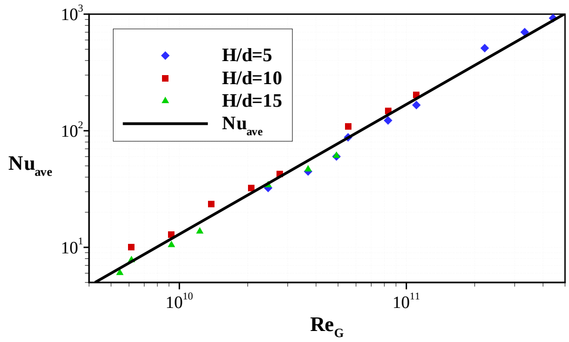

Figure 8: Correlation of $\bar{Nu}$ against Re_G.

Correlation (4) shows a strong dependance of nozzle-to-surface distance H on the averaged Nusselt number.

Furthermore, by studying maximum Nusselt number, we established an exponential based correlation by considering all variables in the general form of eq. (8):

$$Nu_{max} = c_1 M^{c_2}\left(\frac{H}{d}\right)^{c_3}\left(\frac{W}{d}\right)^{c_4} e^{\left[c_5\left(\frac{H}{d}\right)^{c_6}\left(\frac{W}{d}\right)^{c_7}\right]} + c_8 \quad (8)$$

Using multi-variate optimization process to minimizes standard deviation from numerical data, coefficients are determined; resulting in the form of eq. (9) :

$$Nu_{max} = 0.282 M^{0.49}\left(\frac{H}{d}\right)^{-1.69}\left(\frac{W}{d}\right)^{-0.856} e^{\left[9.14\left(\frac{H}{d}\right)^{0.034}\left(\frac{W}{d}\right)^{0.074}\right]} - 3 \quad (9)$$

Correlation (9) shows that nozzle-to-nozzle spacing have negligible effect on the maximum Nusselt number. Indeed, regardless of the nozzle-to-nozzle distance, Nu_{max} is found at the stagnation point. Nu_{max} reflects a strong dependance on jet Mach number.

Kriging Interpolation

To avoid handling several data to establish correlation, we use Kriging method. Even though there are many Kriging techniques to interpolate data, the focus of this study is on dual Kriging [18, 19]. Dual Kriging consist of establishing a derivative function, say $\Phi(X)$, and a fluctuation or covariance function, say $\Psi(X)$. The interpolated function, U, upon the domain X is then represented by eq. (10) .

$$U(X) = \Phi(X) + \Psi(X) \tag{10}$$

The domain upon which we interpolate can be of the form of a one dimensional vector, containing several data points, as well as a multidimensional matrix, for multivariate analysis, as per eq. (11). Variable x_I stands for the vector containing the data points for a specific variable.

$$X = \begin{bmatrix} x_I & x_{II} & x_{III} & ... \end{bmatrix} \tag{11}$$

$$\text{Where} \quad x_I = \begin{bmatrix} x_{I_1} & x_{I_2} & \dots & x_{I_n} \end{bmatrix}^T \tag{12}$$

From a least square point of view, the derivative function stands for the mean value of the function. Although the covariance function lets the Kriging function pass through all sample data points, the derivative function is imperative as it retains the behavior of the data. Most common derivative functions are summarized in Table (3).Typically, a constant or linear derivative function is sufficient when the function steadily evolves and does not show sparse discontinuities.

Table 3: Common derivative forms for dual Kriging

Derivative	Form	
Constant	$\Phi(X) =$	a_0
Linear	$\Phi(X) =$	$a_0 + a_1 x_I + a_2 x_{II} + \dots + a_N x_N$
Quadratic	$\Phi(X) =$	$a_0 + a_1 x_I + \dots + a_N x_N + a_{N+1} x_I^2 + \dots + a_{2N} x_N^2 + a_{2N+1} x_I x_{II} + \dots + a_{2N+N-1} x_I x_N + \dots + a_{2N+N^2-N} x_N x_{N-1}$
Trigo.	$\Phi(X) =$	$a_0 + a_1 \cos(\omega x_I) + \dots + a_N \cos(\omega x_N) + a_{N+1} \sin(\omega x_I) + \dots + a_{2N} \sin(\omega x_N)$

The covariance function reduces locally the standard deviation of interpolated function. A proper covariance function will make the interpolation scheme to pass through all points by correcting the derivative function. By making use of a normalized Eucledian's distance h in the covariance function, the derivative function effect can be segregated. Table (4) summarizes most common covariance forms. Linear, cubic and logarithmic covariance forms behave likely as 1D, 2D and 3D spline-type interpolation. However, Logarithmic covariance form is best suited for multi-dimensional problems [18]. Other covariance forms could be developed as generic forms and could be more suited in case of very sparse sampling. Eqs (15) and (16) show other examples of covariance terms. Fig. (9) shows the effect of different covariance function on the generalized covariance term K.

Table 4: Common covariance forms for dual Kriging

Covariance	Form	
Linear	$K(h) =$	h
Cubic	$K(h) =$	h^3
Logarithmic	$K(h) =$	$h^2 \ln(h)$
Trigonometric	$K(h) =$	$\sin(\omega h)$

$$\text{Thus} \quad \Psi(X) = \sum_{i=1}^{n} b_i K(h_i) \tag{13}$$

$$\text{Where} \quad h_i = |x - x_i| \tag{14}$$

$$K(h) = h^{2p+1} \tag{15}$$

$$K(h) = h^{2p} \ln(h) \tag{16}$$

The dual Kriging problem take the form of a linear system from which we compute the coefficients a's and b's of the derivative and covariance functions. In the case of sparse measurements or to avoid the effect of misleading point, or noise, we can add a weight term to the generalized covariance term K by multiplying the Kriging matrix by a weight factor σ, as per eq. (17). The weight term tends to smooth

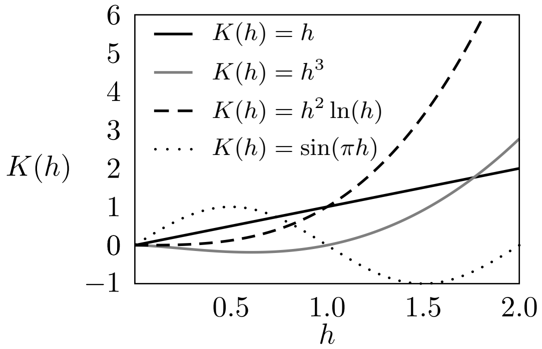

Figure 9: Effect on K using different covariance function

the interpolation scheme, converting the problem to a data fitting scheme ; avoiding explicit fit through all sample points.

$$\hat{\Gamma} = \Gamma + \sigma I \quad (17)$$

$$\text{having} \quad 0 \leq \sigma < h_{max} \quad (18)$$

Having a linear derivative and a logarithmic covariance, the problem takes the form of eq. (19).

$$\tilde{U} = a_0 + \begin{bmatrix} a_1 \\ a_2 \\ a_3 \\ a_4 \\ a_5 \end{bmatrix} \tilde{X} + \sum_{i=1}^{n} b_i K(|\tilde{X} - X_i|) \quad (19)$$

Normalizing parameter vectors by their respective maxima before the evaluation of the Eucledian's distance h ensures a good conditioning of the Kriging matrix Γ or $\hat{\Gamma}$.

Implementation

We make use of the dual Kriging to predict heat distribution from an array of hot-air jets impinging over a curved surface, taking into account the 5 parameters and data from the numerical study.

By making use of a linear derivative and a logarithmic covariance, the dual Kriging linear system takes the form of eq. (20); the domain used reflects the one used in the anti-icing interpolation module.

$$\Gamma \mathbf{x} = \mathbf{f} \quad (20)$$

Where

$$\mathbf{x} = \begin{bmatrix} b_1 \\ \vdots \\ b_n \\ a_0 \\ \vdots \\ a_N \end{bmatrix}, \quad \mathbf{f} = \begin{bmatrix} Nu(X_1) \\ \vdots \\ Nu(X_n) \\ 0 \\ \vdots \\ 0 \end{bmatrix} \quad (21)$$

and

$$\Gamma = \begin{bmatrix} K(h_{ij}) & \cdots & \cdots & 1 & s_1 & y_1 & M_1 & \left(\frac{H}{d}\right)_1 & \left(\frac{W}{d}\right)_1 \\ \cdots & \cdots & \cdots & \vdots & \vdots & \vdots & \vdots & \vdots & \vdots \\ \cdots & \cdots & \cdots & 1 & s_n & y_n & M_n & \left(\frac{H}{d}\right)_n & \left(\frac{W}{d}\right)_n \\ 1 & \cdots & 1 & & & & & & \\ s_1 & \cdots & s_n & & & & & & \\ y_1 & \cdots & y_n & & & & & & \\ M_1 & \cdots & M_n & & & & 0 & & \\ (H/d)_1 & \cdots & (H/d)_n & & & & & & \\ (W/d)_1 & \cdots & (W/d)_n & & & & & & \end{bmatrix} \quad (22)$$

Fig. (10) demonstrates the use of Kriging technique by taking 3 distributions of heat-transfer over curve length s for different Mach numbers. An interpolated curve is calculated for $M = 0.4$ and shows excellent agreement with numerical data. A second interpolated curve is calculated to compute the $M = 0.3$ distribution line.

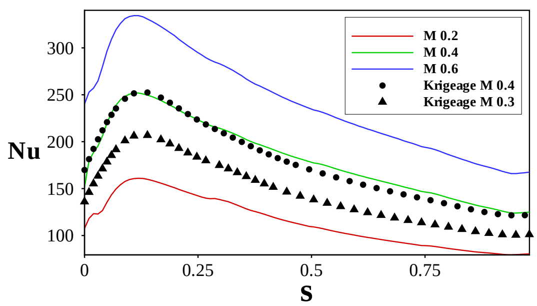

Figure 10: Interpolation using Kriging technique within data of study.

Having a NACA0015 as a 2D profile from root to tip of a wing, we establish the closest circular shape that minimizes standard deviation over 15% of the chord. Then by taking a generic span of 1 meters, a $\frac{H}{d}$ of 10, a $\frac{W}{d}$ of 15 and a jet Mach number of 0.8, we estimate a heat transfer distribution from the multidimensional Kriging method within the results from the numerical study. Fig. (11) shows a representation of interpolated heat transfer from the anti-icing configuration over the curve length s while Fig. (12) shows the representation the interpolated heat transfer over the wing leading edge.

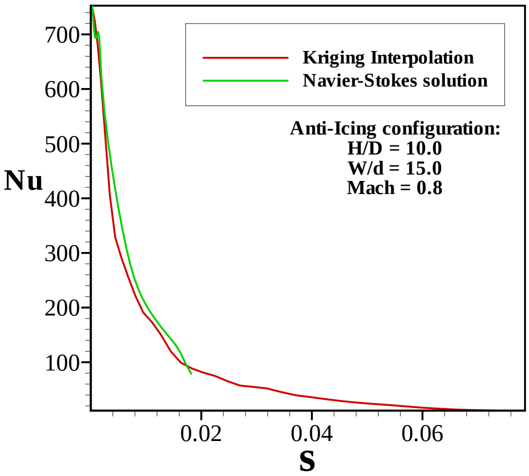

Figure 11: 2D Interpolation over NACA0015 leading edge using Kriging technique.

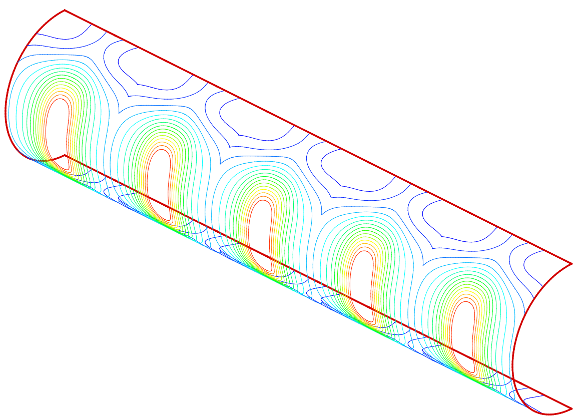

Figure 12: 3D Interpolation over NACA0015 leading edge using Kriging technique.

Conclusion

The paper presented results from a CFD investigation of heat transfer from an array of hot-air jets impinging on a 3D concave (circular) surface.

Correlations has been established for the averaged and maximum Nusselt numbers for different nozzle-to-nozzle spacing, nozzle-to-surface height and hot-air jet mach numbers configurations. Values taken for the numerical study are typical of those for hot-air jets based anti-icing system employed for aircraft wing at Bombardier Aerospace.

A validation case shows good agreement with the experimental data found in the literature.

The dual Kriging interpolation technique has been implemented as a simulation tool for the anti-icing simulation module of CANICE-3D. This scheme interpolates a heat transfer distribution from the CFD result database for a given anti-icing configuration.

The dual Kriging method preserves the non-linear nature of the heat-transfer distribution from hot-air jets impinging over a curved surface and thus is the most clever interpolation scheme for this problem.

Acknowledgement

The authors would like to acknowledge the support of NSERC through a cooperative R & D Grant. Bombardier Aerospace and the Advanced Aerodynamics Group are gratefully acknowledged for their helpful assistance.

References

[1] Federal Aviation Administration. Proceeding. In *FAA International Conference on Aircraft In-Flight Icing*, volume I and II, pages 6–8, Springfield, Virginia, May 1996.

[2] Federal Aviation Administration. FAA in-flight icing plan. Technical report, United States Department of Transportation, April 1997.

[3] F. Morency, F. Tezok, and I. Paraschivoiu. Anti-icing system simulation using canice. *AIAA Journal of Aircraft*, Vol. 36(no. 6):999–1006, Nov.-Dec. 1999.

[4] F. Morency, F. Tezok, and I. Paraschivoiu. Heat and mass transfer in the case of an anti-icing system modelisation. *AIAA Journal of Aircraft*, Vol. 37(no. 2):245–252, Mar.-Apr. 2000.

[5] P. Tran, M.T. Brahimi, L.N. Sankar, and I. Paraschivoiu. Ice accretion prediction on single and multi-element airfoils and the resulting performance degradation. *AIAA Paper 97-0178*, Jan. 1997.

[6] P. Tran, M.T. Brahimi, I. Paraschivoiu, A. Pueyo, and F. Tezok. Ice accretion on aircraft wings with thermodynamic effects. *AIAA Journal of Aircraft*, Vol. 32(no. 2):444–446, 1995.

[7] I. Paraschivoiu, P. Tran, and M.T. Brahimi. Prediction of the ice accretion with viscous effects on aircraft wings. *AIAA Journal of Aircraft*, Vol. 31(no. 4):855–861, July-Aug. 1994.

[8] P. Tran, M.T. Brahimi, and I. Paraschivoiu. Ice accretion on aircraft wings. *Canadian Aeronautics and Space Journal*, Vol. 40(no. 3):185–192, Sept. 1994.

[9] H. Martin. *Heat and Mass Transfer between Impinging Gas Jets and Solid Surfaces*, volume Vol. 13, pages 1–60. Advances in Heat Transfer, academic press edition, 1977.

[10] F. Saeed, F. Morency, and I. Paraschivoiu. Numerical simulation of a hot-air anti-icing simulation. In *AIAA Paper 2000-0630*, volume 2, pages 897–904. 38th Aerospace Sciences Meeting & Exhibit, Jan. 2000.

[11] J.M. Brown, S. Raghunathan, J.K. Watterson, A.J. Linton, and D. Riordon. Heat transfer correlation for anti-icing systems. *AIAA Journal of Aircraft*, Vol. 39(no. 1):897–904, Jan.-Feb. 2002.

[12] C. Meola, G.M. Carlomagno, E. Riegel, and F. Salvato. An experimental study of an anti-icing hot air spray-tube system. *19th Congress ICAS*, Sept. 1994.

[13] G. Croce, W.G. Habashi, G. Guevremont, and F. Tezok. 3D thermal analysis of an anti-icing device using FENSAP-ICE. *AIAA Paper 98-0198*, Jan. 1998.

[14] F. Saeed and I. Paraschivoiu. Numerical correlation for local nusselt number distribution for hot-air jet impingement on concave surfaces. *Proceedings of the 8th Annual Conference of the CFD Society of Canada, CFD2K*, Vol. 2:897–904, June 2000.

[15] M. Fregeau, M. Gabr, F. Saeed, and I. Paraschivoiu. Numerical simulation of heat transfer from an array of hot-air jets impinging on a 3d concave surface. *Proceedings of the 50th CASI Annual General Meeting*, April 2003.

[16] *Fluent 6.0 User's Guide*, Dec 2001.

[17] R. Gardon and J. Cobonpue. Heat transfer between a flat plate and jets of air impinging on it. In *International Heat Transfer Conference*, Pt. 2, pages 454–460, 1961.

[18] F. Trochu. Krigeage en CAO et FAO. Technical report, Ecole Polytechnique de Montréal, Montreal, Canada, Sept. 2001.

[19] Noel A. C. Cressie. *Statistics for Spatial Data*. John Wiley and Sons, 1993.